



TECHNICAL ARTICLE

# The Early-Stage Propagation of Localized Corrosion of a Sintered NdFeB Alloy in Aqueous Environments

Lin Yang, Jialu Ouyang, Zi-Ming Wang, and Guang-Ling Song

Submitted: 18 March 2022 / Revised: 28 January 2023 / Accepted: 10 February 2023 / Published online: 11 July 2023

To capture the initial corrosion of sintered NdFeB alloys, a quasi-in situ investigation of the localized corrosion behavior was conducted in low-conductive aqueous solutions. It was clearly observed that the corrosion pits were started from the active sites in matrix phase adjacent to the phase boundaries and the oxide rings were simultaneously deposited some distance from the pits. The spatial separation of the anode and cathode areas during the corrosion could be explained by the potential-pH diagram of Fe and the transportation of hydroxide and ferrous ions in the solution. Based on the variation of oxide rings with environmental factors, it was deduced that the ring-shaped deposition of corrosion products was cooperatively determined by the ferrous cations from pits and the hydroxide anion generation at the cathodic regions limited by the diffusion of oxygen from the bulk solution. This observation gives new insights into the galvanic corrosion of alloys in aqueous media.

**Keywords** cathode reaction, deionized water, localized corrosion, NdFeB alloy, oxide ring

## 1. Introduction

NdFeB permanent magnetic alloys with low price and high magnetic properties are the preferred materials in the fields of mechatronics, acoustics, biomedicine and so on (Ref 1-3). However, their poor corrosion resistance in various environments greatly limits their commercial applications (Ref 4-6). It is well known that the structural and compositional heterogeneities in NdFeB alloy determine its corrosion resistance (Ref 7, 8). Sintered NdFeB consists of a multiphase structure, mainly including the main phase Nd<sub>2</sub>Fe<sub>14</sub>B, Nd-rich phase Nd<sub>4</sub>Fe and B-rich phase Nd<sub>1+ε</sub>Fe<sub>4</sub>B<sub>4</sub> (Ref 9). Obviously, the galvanic coupling effect among these heterogeneous phases (Ref 10, 11) would play a key role in determining the corrosion resistance of NdFeB alloys when exposed to aqueous electrolytes in application. It is important to reveal the galvanic coupling effect on NdFeB alloy surfaces.

Owing to the high activity of Nd element, the Nd-rich grain boundaries would be preferentially oxidized or etched (Ref 11,

12). The Nd-rich phase acted as the anode when it was coupled with the Fe-rich main phase, performing an intergranular corrosion morphology on NdFeB alloy surfaces (Ref 10, 13, 14). It was generally believed that localized attacks started at the Nd-rich phase and then propagated along the grain boundaries (Ref 11, 12, 15). However, the electrochemical activity of the Fe-rich, Nd-rich and B-rich phases of NdFeB alloys would be changed with exposure environments (Ref 16, 17), such as the pH value, the concentration of chloride ion and other environmental factors in aqueous electrolytes (Ref 13, 18, 19). For example, the Nd-rich phase was more corrosion resistant than the matrix phase in solutions with a pH value higher than 5, while the Fe-rich phase presented much nobler in acidic solutions (Ref 15). It seemed that the Nd oxides possibly performed a better protectiveness in a nearly neutral or alkaline solution (Ref 15). It has been reported that the Nd-rich phase at the grain boundaries was not preferentially dissolved in some immersion tests, while the Fe-rich main phase was obviously corroded (Ref 16). This could be attributed to the highly stable Nd oxides preformed or inherently covered on the Nd-rich phase (Ref 16). The main phase may also contain some weak points for the initiation of localized attacks (Ref 20). It seems that the localized corrosion of NdFeB alloys would be influenced by the alloy structure and the environmental factors. Currently, conflicting results were reported on the corrosion behavior of NdFeB alloys and there were lack of direct observation of the initial stage of corrosion.

The corrosion of NdFeB alloy is a result of the cooperation of the anodic and the cathodic reactions on alloy surfaces. During corrosion, these active sites would be spatially varied with time. Without polarization, the anodic reaction currents equal to the cathodic reaction currents on the alloy surface. The anode area was rather localized with a small fraction to the whole surface. A strong galvanic effect between the small anode and the large cathode was generally produced (Ref 21, 22). In aqueous environments, the Nd<sub>2</sub>Fe<sub>14</sub>B matrix phase may act as the cathode (Ref 10, 15), absorbing oxygen for reduction. However, there is still lack of evidence on the spatial

Lin Yang, Jialu Ouyang, and Zi-Ming Wang, Center for Marine Materials Corrosion and Protection, College of Materials, Xiamen University, Xiamen 361005, China; and Guang-Ling Song, Center for Marine Materials Corrosion and Protection, College of Materials, Xiamen University, Xiamen 361005, China; Department of Ocean Science and Engineering, Southern University of Science and Technology, Shenzhen 518055 Guangdong, People's Republic of China; State Key Laboratory of Physical Chemistry of Solid Surfaces, Xiamen University, Xiamen 361005, China; and School of Mechanical and Mining Engineering, The University of Queensland, St. Lucia, QLD 4072, Australia. Contact e-mails: zmwang@xmu.edu.cn and guangling.song@hotmail.com.

distribution of the cathode region and its relationship with the phases in NdFeB alloys. In humid atmosphere, some crater-like corrosion morphologies could be observed (Ref 23), which was attributed to the accumulation of micro-droplets on NdFeB surfaces. This phenomenon was similar to the corrosion induced by Evans droplets (Ref 24, 25), where the cathodic reactions mainly occurred at the water/air interface because of oxygen gradients. Identifying the spatial distribution of cathode reactions is crucial to uncover the local galvanic corrosion mechanism of NdFeB alloys.

In this paper, we focused on the localized corrosion phenomenon of NdFeB alloys. The experiments were designed to explore the governing mechanism for the initiation and propagation of localized corrosion. As the high corrosion rate of NdFeB alloys in aqueous solutions, most studies reported a well-developed corrosion stage, in which the NdFeB surface was completely damaged even after a short period of exposure (Ref 13, 14, 16, 26–28). To slow down the corrosion process, low-conductive deionized water (Ref 16, 19) or other low-conductive solutions were used in this study. At the same time, a quasi-in situ SEM method was used to observe the corrosion morphology with an immersion interval from tens of seconds to several minutes. Based on the above attempts, the early-stage propagation of localized corrosion on NdFeB surface associated with the variation of environmental factors was clarified, further exploring the local galvanic corrosion on heterogeneous NdFeB alloy surfaces.

## 2. Experiments

### 2.1 Material and Solution

The NdFeB alloy was sintered using commercial powder with a composition of Nd: 32, Fe: 64, B: 1 wt.%, and the bonding agents ~ 3 wt.%. The heterogeneous microstructure governs the galvanic corrosion behavior of NdFeB alloy. For a better observation of the galvanic corrosion, the sintered NdFeB alloy was thermally treated to obtain a larger Nd-rich phase. In this experiment, to clearly identify the Nd-rich phase, the sintered NdFeB was firstly heated to 900 °C keeping for 60 min and then cooled to 500 °C annealing for 120 min in an argon gas-protected furnace. Finally, the sample was cooled to room temperature in the furnace. The NdFeB alloy samples were sealed in epoxy resin with an exposure area of 1 cm × 1 cm for corrosion tests. The NdFeB sample was successively grinded with 400#, 1200#, 2000# and then polished to a mirror surface. To avoid corrosion during sample preparation, anhydrous ethanol was used as the polishing agent. The NdFeB samples used for corrosion tests were prepared from one large heat-treated sample, holding a similar distribution of Nd-rich phase in the NdFeB alloy.

The solutions for corrosion tests include deionized water, ethanol–water mixtures, ethanol–brine mixtures and alkaline solutions. The ethanol–water mixture was prepared using deionized water with an ethanol fraction of 75, 90 and 99%, and the ethanol–brine mixture was prepared by mixing 0.01 mol/L NaCl solution with ethanol. One purpose of using these low-chloride solutions was to slow down the active dissolution of NdFeB alloy, facilitating the observation of galvanic corrosion phenomena at the microscales. The pH value of the alkaline solution was adjusted by using 0.1 mol/L NaOH aqueous solution.

### 2.2 Immersion Test

The NdFeB sample was immersed in different electrolytes for corrosion tests. In each test, the solution volume was about 100 mL. The sample surface for corrosion test was parallel to the liquid level and was placed at 1 cm below the solution/air interface. The samples were corroded for different immersion periods. Once the sample was picked out from the solution, it was quickly cleaned with ethanol and dried with Ar gas flow. Each test was conducted on three parallel samples.

Without specific statement, the immersion test was measured at room temperature (25 °C). The 80 °C immersion tests in 75% ethanol–water solution were performed in a chamber with controllable temperature and humidity.

### 2.3 Electrochemical Methods

Electrochemical measurements were conducted using a Gamry electrochemical workstation in a three-electrode system, where a platinum sheet was used as the counter electrode and a saturated calomel electrode (SCE, KCl) as the reference electrode. The electrochemical measurements were conducted in deionized water. Before the potentiodynamic polarization test and the EIS measurement, the NdFeB sample was initially immersed in the solution for 600 s, until the open-circuit potential (OCP) became stable. The potentiodynamic polarization curves were swept from -0.5 V to + 0.5 V vs. OCP with a scanning rate of 1.0 mV/s. The EIS measurement was conducted at OCP with  $\pm 5$  mV AC perturbation in the frequency from  $10^5$  to 0.01 Hz, and the acquisition rate was 4 points/decade. All the tests were repeated for three times.

To enhance the anode or cathode reactions on NdFeB alloy surfaces, a positive or negative potential vs. OCP was intermittently applied. In a cycle of one minute, the electrode was firstly kept at OCP for 40 s and then it was polarized for 20 s. Generally, 10 cycles were conducted for surface morphology observation. We selected several applied potentials ranging from - 0.3 to + 0.3 V vs. OCP to magnify the influence of anode or cathode reactions on surface morphology.

### 2.4 Quasi-in situ SEM Observation

The as-polished NdFeB sample was ultrasonically cleaned in anhydrous ethanol, dried with argon, and then immediately placed into the chamber of scanning electron microscope (SEM, Phenom XL). The SEM observation was conducted under an electron-accelerated voltage of 15 keV in back-scattering diffraction (BSD) mode. Firstly, the original surface before immersion tests was observed by using SEM to identify a featured region according to the phase distribution on NdFeB alloy surface. This featured region was repetitively investigated in the following SEM observation after immersion tests, which was defined as a quasi-in situ SEM test. The location and direction of NdFeB samples in SEM chamber were carefully fixed in each test. After immersion test, the NdFeB sample was immediately washed with ethanol and dried with Ar gas flow. The process kept for less than 1 min before placing the NdFeB sample into the SEM chamber, to avoid possible corrosion or oxidation in air. At the initial stage, the time interval of the immersion test in a quasi-in situ observation was 10 s, 30 s and 1 min. At a later stage, the immersion interval time was 5 and 10 min, and finally it was stopped after a total immersion time of 40 min. The temperature in the laboratory was kept around 25 °C, and the humidity was about 82%.

## 2.5 Surface Characterization

The phase distribution on NdFeB alloy surface before and after immersion tests was analyzed by the mapping mode of energy-dispersive spectroscopy (EDS, Phenom XL). Laser Raman spectrometer (Horiba XP) was applied to analyze the component and composition of the corrosion products after immersion tests using a 50X objective. Raman excitation was performed with a Torus single-frequency laser beam with a wavelength of 532 nm and a laser spot diameter of 2-3  $\mu\text{m}$ . A very low laser power of 0.1 mW was adopted to avoid damaging the corrosion products. A stereomicroscope (Leica DVM6) was used to capture the typical galvanic corrosion morphologies on NdFeB surface under a 3D mode. X-Ray diffraction (XRD, D8-A25) with a scanning rate of 0.01 degree/step was used to identify the structure of NdFeB using Cu  $K_{\alpha}$  radiation.

## 2.6 Other Analytical Methods

The solution conductivity was measured by the conductivity meter (Mettler Toledo), as summarized in Table 1. The resistivity of NdFeB substrate was measured using a Chroma Digit Multimeter. The concentration of chloride ion remained in the deionized water was 3.36 mg/L as determined using ion chromatography (DIONEX, ICS-600). The concentration of oxygen in solutions was detected using a trace dissolved oxygen meter (LB-RJY03) with a detection limit of 0.01 mg/L. At 25 °C, the concentration of oxygen in deionized water was 6.38 mg/L. At 80 °C, the concentration of oxygen in deionized water was 2.17 mg/L.

## 3. Results

### 3.1 An Early Initiation of Corrosion

Figure 1 shows the typical structural characteristics of an NdFeB alloy. The SEM image in Fig. 1a presents a two-phase structure, in which the bright area is the Nd-rich phase, and the dark gray area is the matrix phase. The EDS maps in Fig. 1b and c illustrate the distribution of phases in NdFeB alloy. Some areas of the Nd-rich phase became round and continuous at the triple junctions of phase boundaries. Others seem like white stringers located at the two-phase boundaries. According to the XRD pattern in Fig. 1d, the matrix phase is  $\text{Nd}_2\text{Fe}_{14}\text{B}$  (ICDD: 04-006-3646). No Nd-rich or B-rich phase could be detected from XRD, as their relatively low fractions in the NdFeB alloys.

A featured micrograph was selected to observe the initiation of corrosion on NdFeB alloy surface. It seems that the early

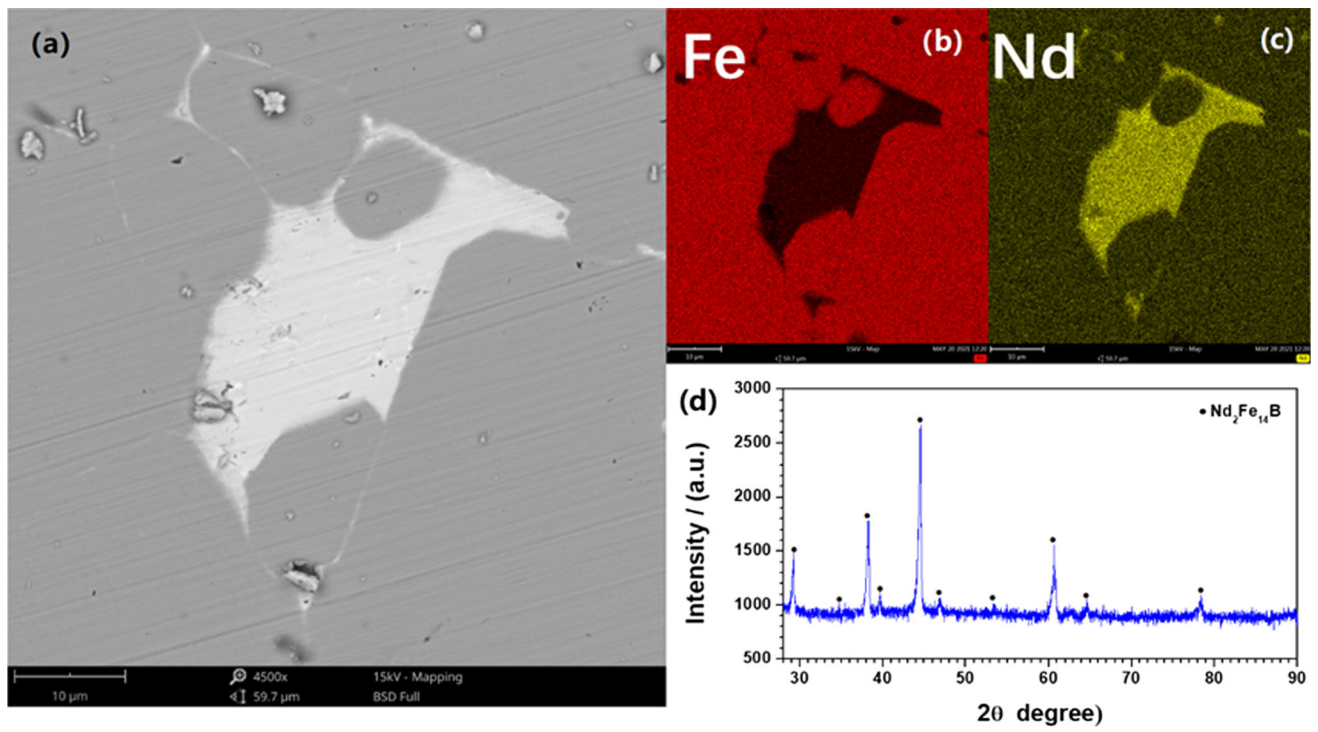
corrosion preferentially initiates at the places associated with the Nd-rich phase boundaries. As seen in Fig. 2a, some inclusions, crevices and holes are also observed on the NdFeB surface. Corrosion was prone to initiating in these sites. After immersion in deionized water for 1 min (Fig. 2b), some tiny pits appeared at the matrix phase near to the phase boundary of the Nd-rich phase and the main phase. At this stage, the typical size of a single pit was less than 1.0  $\mu\text{m}$ . With increasing immersion time, these local small pits expanded to the main phase and then merged into larger ones, as shown in Fig. 2c. After immersion for 3 min (Fig. 2d) and 10 min (Fig. 2e), some black corrosion products were deposited on the matrix phase surface with a certain distance away from these pitted regions. EDS analysis confirmed that the black particles were a mixture of Fe oxides and Nd oxides, where the atomic mass percentage of Fe was 35.68% and that of Nd was 13.52%. After immersion for 40 min (Fig. 2f), the main phase near the phase boundary was dramatically corroded. However, the Nd-rich phase almost maintained its original shape on NdFeB surface, indicating a rather weak corrosion.

Figure 3a presents the locally magnified image of a corroding NdFeB surface, from which the initiation and propagation of pits were clearly shown. The inserted spits indicated the growing edges of the newly generated or the merged pits. After 1 min of immersion, some single pits were separately initiated at the Fe-rich substrate just adjacent to the Nd-rich phase. After 2 min of immersion, these pits grew larger and merged together, as a result of the active dissolution of the pit edges. After 3 min of immersion, there was no single pits could be identified and a large crater was generated, leaving a strip Nd-rich phase beside the corroded areas. The original state of the Nd-rich strip was indicated in a red rectangle in Fig. 2a. After 5 min of immersion, the crater broadened to larger one. Finally, after 10 min of immersion, the crater further propagated and some new pits were combined together. During the fast propagation of the local craters, the Nd-rich phase almost keeps undissolved, as indicated from the white gray strips in Fig. 3a.

The electrochemical activity of NdFeB surface may be varied during the initiation of corrosion pits. As seen from Fig. 3b, the open-circuit potentials of NdFeB alloy in deionized water gradually become stable within 300 s, keeping at  $-0.725$  V vs. SCE during the immersion test. The gradual decrease of OCP revealed the enhanced activity of the NdFeB substrate, during which some micro-pits were generated. In deionized water, the free corrosion current density was about  $3.6 \times 10^{-6}$  A/cm<sup>2</sup> according to fitting the anodic and cathodic curves, as illustrated in Fig. 3c. It should be noticed that the deviation from linearity in the Tafel region could mainly be caused by the high resistivity of the deionized water. In the EIS plot in Fig. 3d, a typical reactive electrode behavior related to the dissolution of NdFeB surfaces is presented, as illustrated in the inserted equivalent circuit in Fig. 3d, where  $R_{ct}$ ,  $R_s$  and  $Q_{dl}$  are the charge transfer resistance, the solution resistance and the capacitance of double layer, respectively. In badly conductive deionized water,  $R_s$  and  $R_{ct}$  can be estimated by curve-fitting to be 3441 and 2479  $\Omega\cdot\text{cm}^2$ , respectively. The former is even higher than the latter. In this case, without IR-drop compensation, the polarization curve will not exhibit a typical Tafel linear region (see Fig. 3c). During immersion tests, the electrode was not stable as expected, and some scattered data points at low frequencies in the EIS plot might be caused by local corrosion reactions. The electrochemical results were

**Table 1** Conductivities of the electrolyte solutions used in this paper

Solution	Conductivity, $\mu\text{s}/\text{cm}$
Deionized water	34.3 $\mu\text{s}/\text{cm}$
75% $\text{C}_2\text{H}_5\text{OH}$	3.3 $\mu\text{s}/\text{cm}$
0.01 mol/L NaCl with 75% $\text{C}_2\text{H}_5\text{OH}$	335.0 $\mu\text{s}/\text{cm}$
0.01 mol/L NaCl with 90% $\text{C}_2\text{H}_5\text{OH}$	237.3 $\mu\text{s}/\text{cm}$
0.01 mol/L NaCl with 99% $\text{C}_2\text{H}_5\text{OH}$	210.0 $\mu\text{s}/\text{cm}$



**Fig. 1** SEM, EDS maps and XRD of the sintered NdFeB alloy

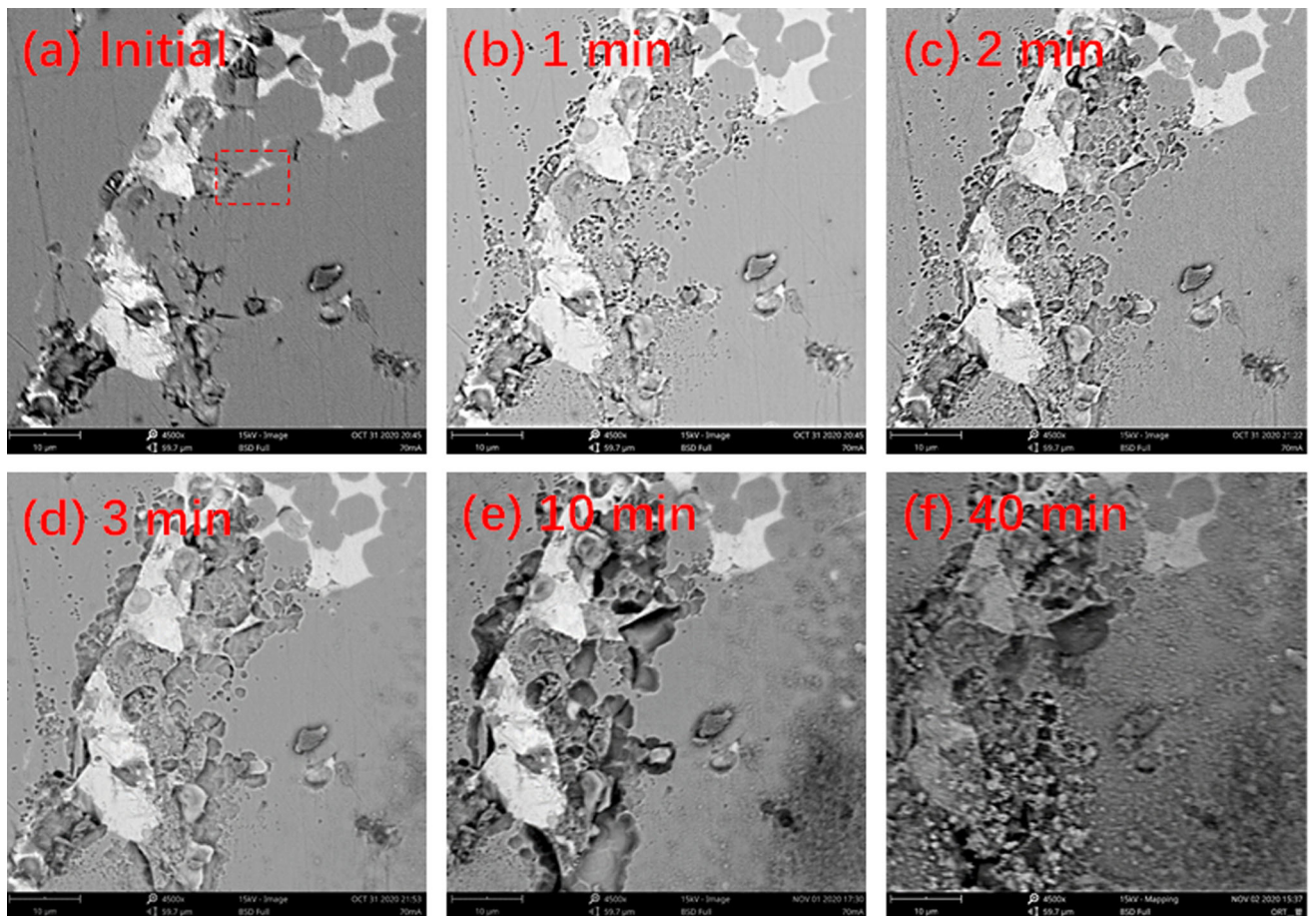


**Fig. 2** SEM observation of the corrosion initiation on typical NdFeB alloy surfaces in deionized water

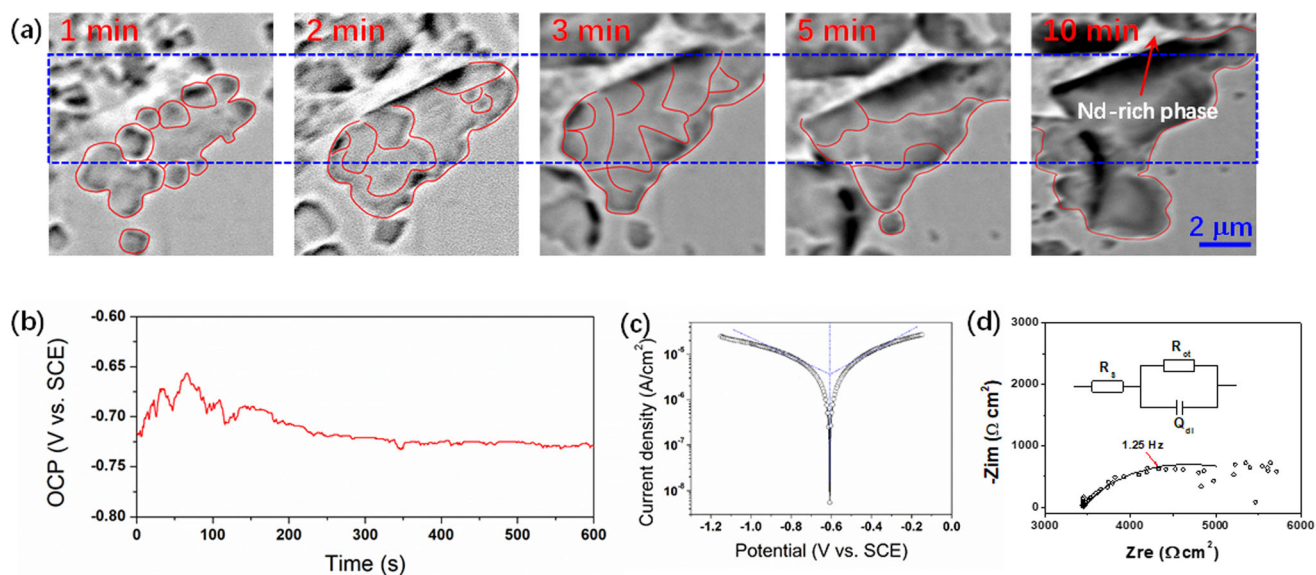


**Fig. 3** The developing pits and the electrochemical curves of NdFeB alloy in deionized water: (a) Magnified images of pit morphology as a function of immersion time, taken from the marked red-dash rectangular area in Fig. 2, (b) open-circuit potential (OCP), (c) potentiodynamic polarization curve and (d) Electrochemical impedance spectroscopy (EIS) Nyquist plot

consist with the quasi-in situ observation of the early corrosion morphology of NdFeB alloy surface in Fig. 2.

It should be noticed that pits were in the matrix phase near to the phase boundaries, other than in the Nd-rich phase as expected. Although the free corrosion potential of Nd-rich phase was lower than that of the matrix phase, the presence of stable Nd oxides could completely cover the Nd-rich phase in deionized water with a pH value of 6.48, resulting in little difference in the potential between the Nd-rich phase and the matrix phase (Ref 15). As a result, the Nd-rich phase did not act as the anode in galvanic corrosion. The phase boundary became more active than the Nd-rich phase due to the defects and local stress (Ref 7, 20). Therefore, the active sites near to the phase boundary were preferentially dissolved as anode pits in corrosion.

### 3.2 Deposition of Corrosion Products

Figure 4 shows the SEM images with a large-field vision of the corroded NdFeB alloy surfaces. Some corrosion products around the pits gradually appeared on NdFeB surface with immersion time. After immersion in deionized water for 10 min, many dark rings appeared far away from the pitted areas. As mentioned in Sect. 3.1, these dark rings are corrosion products composed of Fe and Nd oxides. From the normal distribution of the radius of the oxide rings formed on NdFeB surface in deionized water (Fig. 4b), its mean value was 32.6  $\mu\text{m}$ .

Next, we characterized the localized corrosion morphology in more detail. The 3D morphology of a typical pitted area is shown in Fig. 5. It can be seen that the pitting area was sunken from the original surface, which was surrounded by the ring-like deposits of corrosion products. The depth of the pitted area was about 1.0  $\mu\text{m}$ , and the height of corrosion product deposits was about 4.5  $\mu\text{m}$  from the original surface. Obviously, the galvanic corrosion morphology on NdFeB in immersion conditions is similar to the corrosion morphology under an Evans droplet, showing similar ring-shape distribution of the

corrosion products around the anode area (Ref 24). As observed in Sect. 3.1, the dissolved Fe and Nd from the active sites in the Fe-rich main phase near to the phase boundaries leave a concave developed from the merged corrosion pits. After releasing sufficient  $\text{Fe}^{2+}$  ions from the pitted area, the corrosion products would be deposited on the NdFeB surface. The reason for the deposition some distance away from the anode area, not in the adjacent zone, will be given later.

With prolonging immersion time in deionized water, the corrosion products gradually changes from gray to dark (Fig. 6), indicating the formation of thicker oxide rings. However, the averaged radius of the oxide rings keeps unchanged with time, locating in a range of 38–44  $\mu\text{m}$ , as statistically measured in Fig. 6. It indicates that the gradual release of  $\text{Fe}^{2+}$  with time is not the controlling factor for the deposition of oxide rings, which possibly relies on the cathodic reactions.

### 3.3 Surface Composition Distribution

The composition distribution around the pitted area was further determined using the EDS mapping analysis and the laser Raman spectra, as illustrated in Fig. 7. On EDS maps, O element is mainly distributed along the corrosion product rings, Fe element is uniformly distributed on the surface and Nd element is mainly observed at the Nd-rich phase. Fe element in the oxide ring region was slightly deficient because of the reduction of relative ratio to oxygen. The bright spots (labeled D) was detected as Nd oxides as shown in the table of Fig. 7b. Figure 7c shows the Raman spectra from the regions labeled A, B and C in Fig. 7a, where they reference to the anode pit, the blank region and the oxide ring, respectively. It seems that  $\text{Fe}_2\text{O}_3$  mainly existed at the oxide rings. In the anode region, the  $\text{Fe}_2\text{O}_3$  peaks are very weak. No obvious peak was derived from Nd oxides in Raman spectra, possibly due to the amount of Nd oxides below the detection limits.

The anode region could successively releases  $\text{Fe}^{2+}$  ion as the pitting proceeds.  $\text{Fe}^{2+}$  ion diffusion away from the anode region

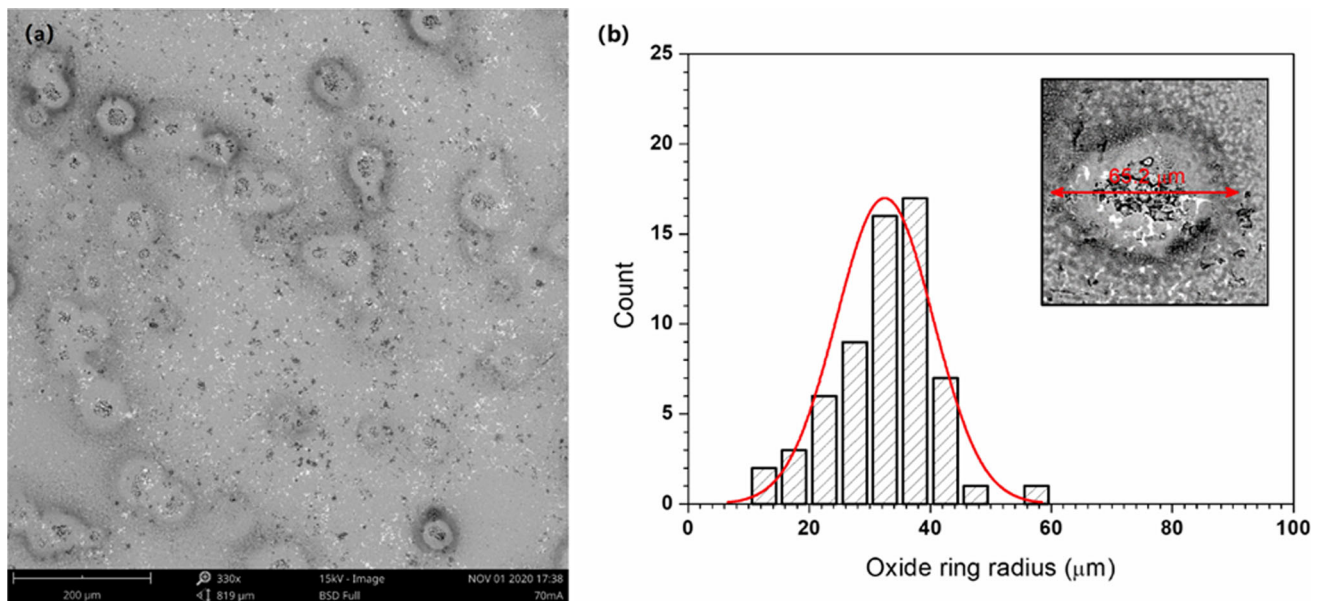


**Fig. 4** Surface morphology of NdFeB alloy samples after immersion in deionized water at room temperature for 10 min. (a) SEM image, (b) the normal distribution of radius and a typical illustration of the oxide rings

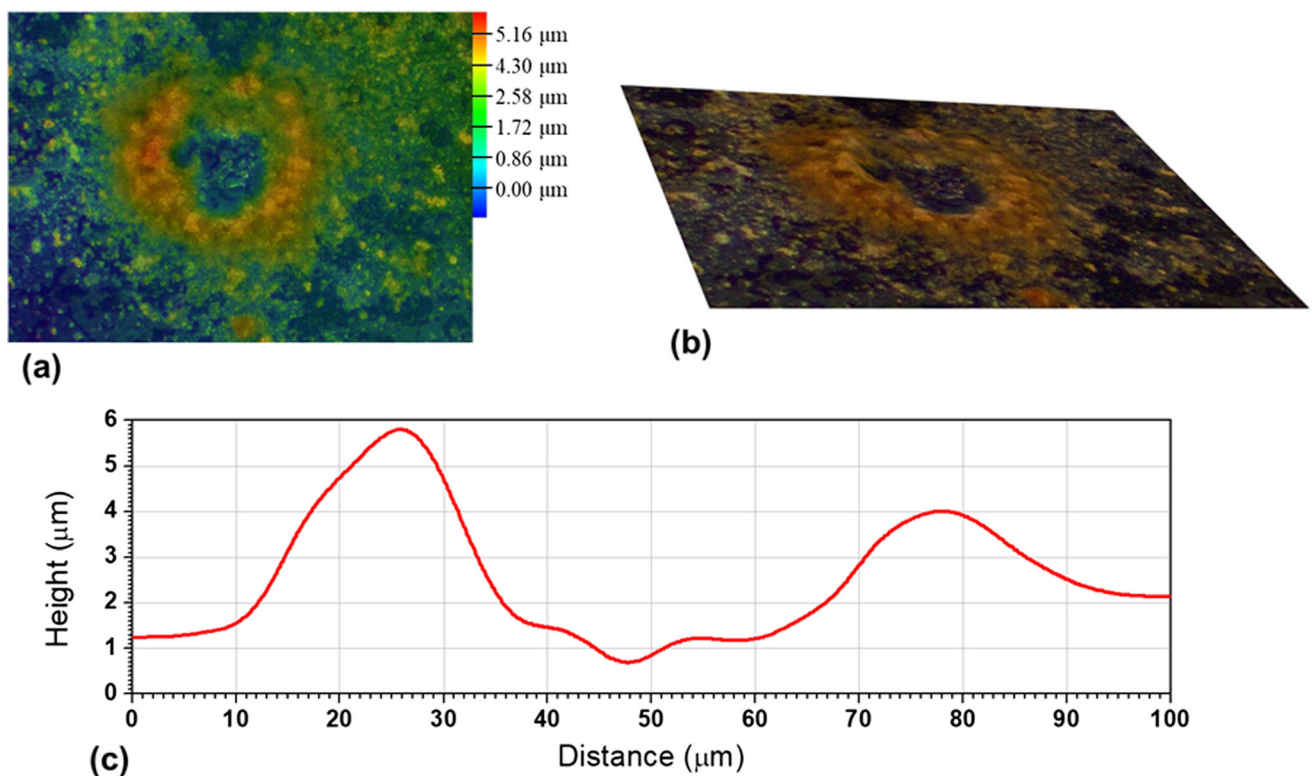


**Fig. 5** Characterization of localized corrosion on NdFeB alloy surfaces. (a) 2D and (b) 3D surface morphology and (c) the depth profile of a single crater and its surrounding oxide ring

was driven by the high concentration gradient. Simultaneously, the cathode reaction for oxygen reduction occurred on the entire alloy surfaces. When the concentrations of  $\text{Fe}^{2+}$  and  $\text{OH}^-$  reached their solubility limits, deposition of corrosion products occurred. Owing to the heterogeneous distribution of  $\text{OH}^-$  ion adjacent to alloy surfaces, the corrosion products were prone to deposit on the regions where the concentration product of  $\text{Fe}^{2+}$

and  $\text{OH}^-$  ions was high enough. Therefore, the oxide rings observed in SEM images indicated the local accumulation of  $\text{OH}^-$  and  $\text{Fe}^{2+}$ , resulting from the cathodic reactions and anodic dissolution. From EDS maps (Fig. 7a), it seems that oxygen was rather deficient on the Nd-rich phase, indicating the significantly depressed deposition of corrosion products. Such a local variation of surface composition was related to the

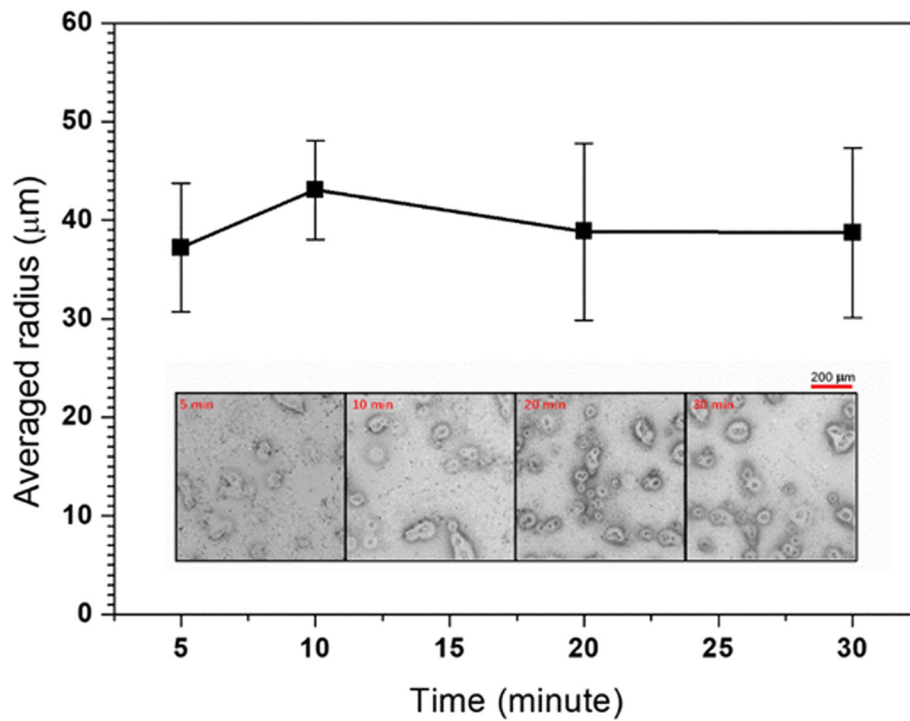


**Fig. 6** The averaged radius of the oxide rings and the typical images of the corrosion morphology (the inserted figures) on NdFeB alloy surface as a function of immersion time in deionized water

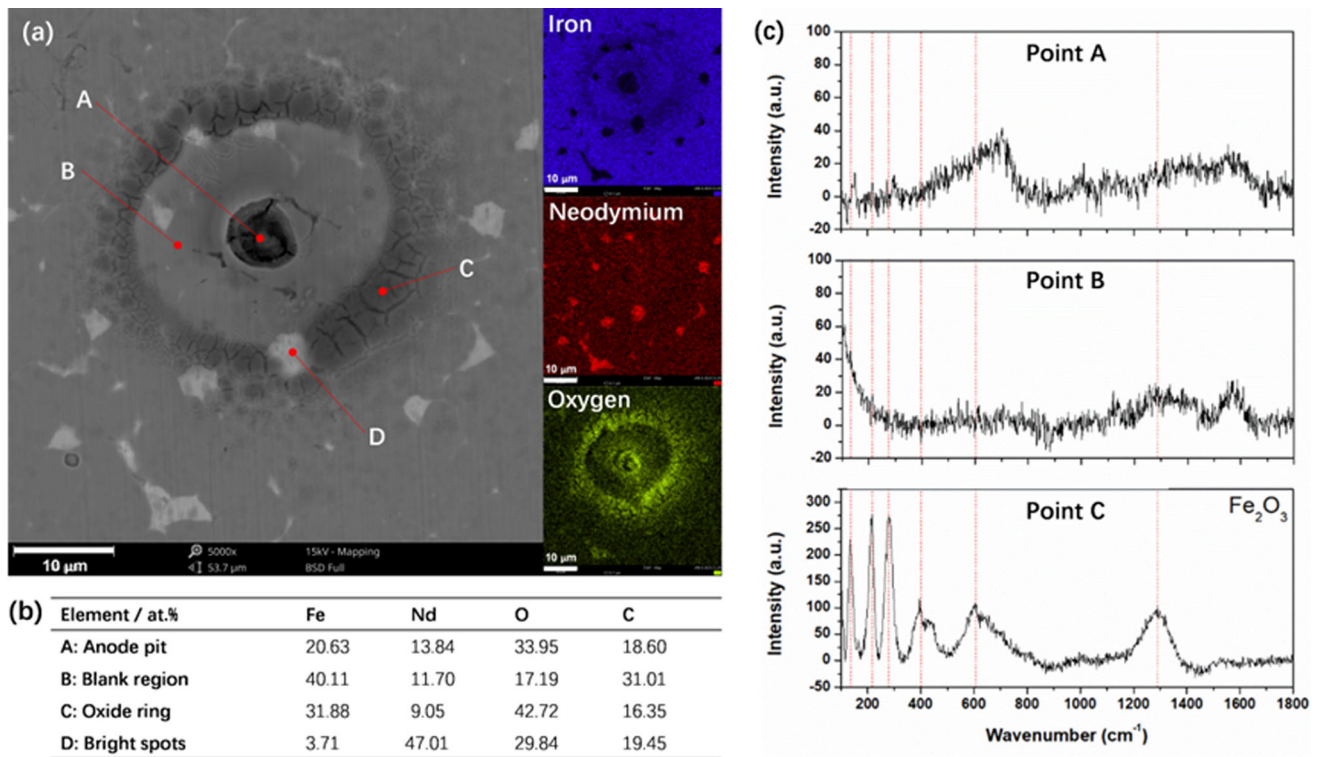


**Fig. 7** Typical illustration of a single crater/pit and its surrounding corrosion products on NdFeB alloy surfaces after immersion in deionized water for 10 min. (a) SEM images and EDS maps; (b) Elemental concentrations detected by EDS of point A, B, C and D in (a); (c) the Raman spectra of Point A, B and C in (a)

heterogeneous structure of NdFeB alloys. Generally, Nd-rich phase is badly conductive compared to matrix phase. The low conductivity of the Nd-rich phase could locally hinder the cathode reaction.

### 3.4 Sensitivity to Environmental Variations

The formation of oxide rings on steel under Evans droplet is contributed to the oxygen concentration gradient in the droplet (Ref 24). In immersion conditions, there is no obvious oxygen gradient in the bulk solution near to the NdFeB alloy surface. The cathode reactions would homogeneously happen on the surfaces aside the active anode area, performing a large cathode area relative to the small anode area. However, the corrosion products were restricted in a ring-shaped region (Fig. 4), indicating a localization of the deposition of  $\text{Fe}^{2+}$  and  $\text{OH}^-$ . We tried to figure out the factors influencing the distribution of cathode regions by changing the experimental environments.

**3.4.1 Solution Conductivity.** To isolate the influence of electrolyte conductivity on the initial localized corrosion morphology on NdFeB surfaces, the immersion experiments were conducted in ethanol-brine mixtures with varying water fractions. Their corresponding conductivities were given in Table 1. Although the concentration of chloride ion was similar, a higher conductivity assists the early identification of anodic pits and oxide rings. For example, the oxide rings can be clearly identified on NdFeB surface after immersion for 10 min for the 90% ethanol-brine solution, but it needs tens of minutes for the 99% ethanol-brine case. Therefore, the SEM images used for the statistical analysis were derived from the samples immersed for 370 min in the 99% case, while immersion for 20 min was chosen in other cases. As shown in Fig. 8, the radius of the oxide ring was almost unchanged when the solution conductivity was less than 200  $\mu\text{S}/\text{cm}$ . The radius is similar to that of oxide rings in deionized water (with the conductivity of 34.5  $\mu\text{S}/\text{cm}$ ). It gradually increased when the solution conductivity was higher than 200  $\mu\text{S}/\text{cm}$ . This is reasonable, as the galvanically protected zone is well known to be increasing with increasing conductivity of solution (Ref 29). In a highly conductive solution, the ferrous ion could be more easily driven by the galvanic current to farther locations to combine with the

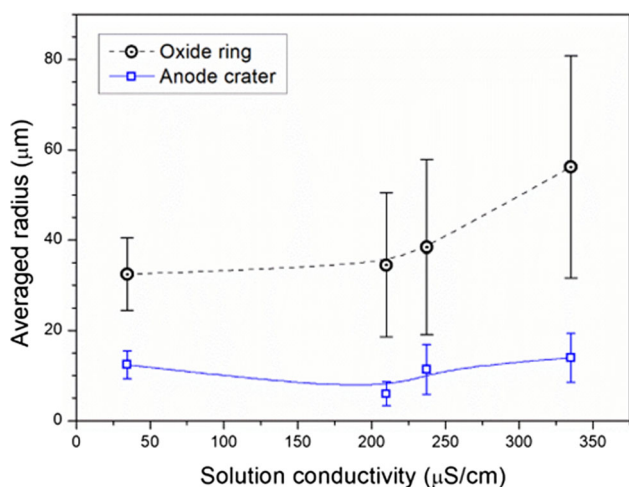


**Fig. 8** The averaged radius of the oxide rings and the anode craters on NdFeB alloy surfaces as a function of solution conductivity

hydroxides generated from cathodic areas.

**3.4.2 Oxygen Concentration.** Although there was no oxygen gradient in immersion tests, if the consumption of oxygen was fast during corrosion, a concentration gradient was built between the locally active site and the bulk solution. To testify the influence of dissolved oxygen on the geometry of the oxide rings, we generated an oxygen-deficient and an oxygen-abundant bulk solution relative to the normally used deionized water by  $\text{N}_2$  bubbling for 20 s and  $\text{O}_2$  bubbling for 20 s, respectively. The concentrations of dissolved oxygen in the oxygen-deficient and oxygen-abundant water were around 2.0 and 8.0 mg/L, respectively. It was clear that the oxide rings were significantly enlarged with increasing oxygen concentration (Fig. 9). This was because more hydroxides could be generated in farther areas to participate in the deposition of corrosion products when the solution contained a higher level of oxygen. For the oxygen-abundant condition, we noticed that the width of the oxide rings was also broadened, where the distance between the plateau of the inner ring side and its outer edge (as indicated by the blue point in Fig. 9) was over 20  $\mu\text{m}$ . This could be attributed to the sustaining supply of oxygen to cathode reaction sites. For the oxygen-deficient condition, the radius of oxide ring became smaller compared to the original ones formed in deionized water. It was possible that oxygen could only sustain the cathode reactions in a smaller space, as the corrosion reactions were controlled by diffusion of oxygen from the bulk solutions.

**3.4.3 Solution Temperature.** The size of the oxide rings was diminished with increasing solution temperatures. Figure 10 shows the distributions of the oxide rings derived from the SEM surface morphologies of NdFeB samples after immersion in 75% ethanol-brine solution at room temperature and 80  $^{\circ}\text{C}$ , respectively. The typical oxide rings were illustrated as inserted figures. As seen from Fig. 10a, after immersion in 75% ethanol-brine solution for 10 min at room temperature, the mean radius of the oxide rings was 38.6  $\mu\text{m}$ , which had no obvious change compared with that observed in deionized water (32.6  $\mu\text{m}$  in Fig. 4). When the temperature increased to 80  $^{\circ}\text{C}$ , the mean radius of the oxide rings greatly reduced to 11.99  $\mu\text{m}$ , as shown in Fig. 10b. With increasing temperature from room temperature to 80  $^{\circ}\text{C}$ , dissolved oxygen in the 75% ethanol-brine solution was decreased from 11.68 to 1.98 mg/L, changing the corrosion kinetics of the cathode reactions and reducing the size of oxide rings. It should be noticed that the electronic resistivity of NdFeB substrate was also significantly increased from 10-80 to 200-400  $\Omega\cdot\text{cm}$ , with heating the sample from room temperature to 80  $^{\circ}\text{C}$ . The widely scattered electronic resistivity may be owing to the defective sintered structure and the heterogeneous surface conductivity. Besides the influence of oxygen concentrations, there may be some links between the size of the oxide rings and the electronic resistivity of the alloy substrate. A bad conductivity hindered the cathode reactions on NdFeB surface, as the migration of electrons was closely relied on the surface conductivity. This assumption was verified by the mitigated deposition of corrosion products on the badly conductive Nd-rich phase (Fig. 5). The high resistivity of NdFeB substrate hindered the electron transfer from anode to cathode, thus reducing the radius of the cathode reactions.

**3.4.4 Applied Potential.** To confirm the dependence of the oxide rings on the cathodic hydroxides and anodic ferrous ions, the NdFeB surfaces were alternately applied with



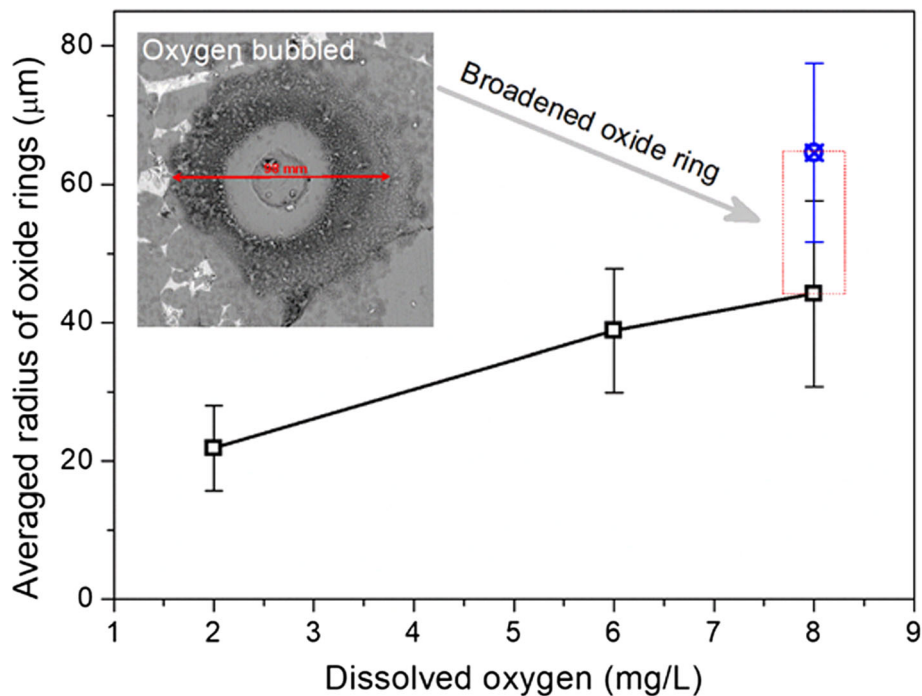


**Fig. 9** The averaged radius of the oxide rings on NdFeB alloy surfaces as a function of dissolved oxygen concentration in deionized water

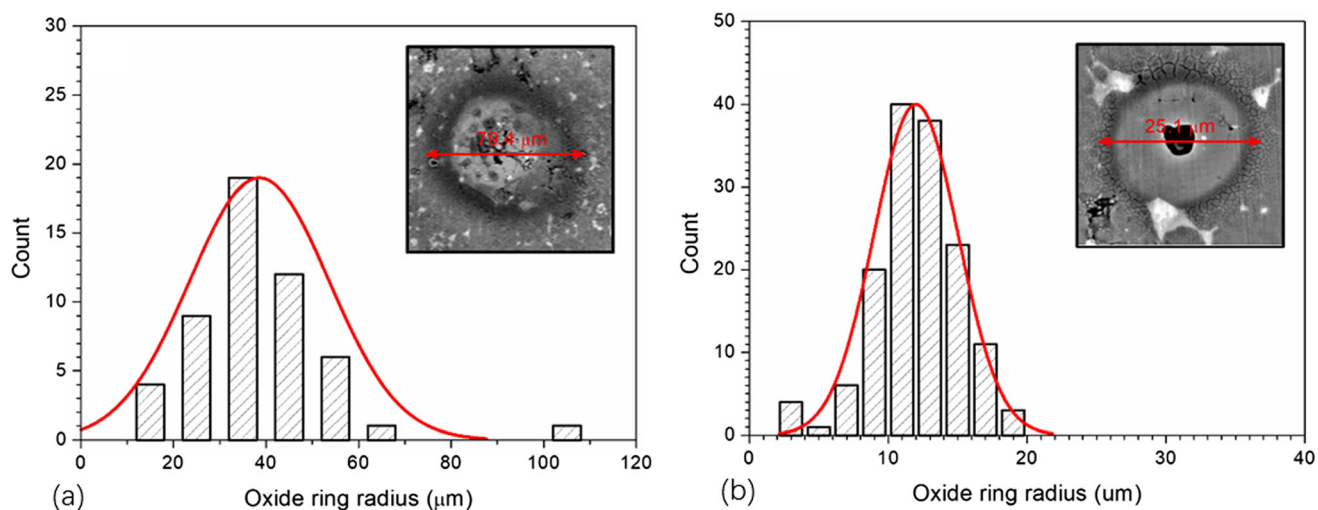


**Fig. 10** Histogram of the oxide ring radius and the typical illustration of a single oxide ring (inserted figure) of NdFeB alloy samples after immersion in 75% ethanol–water solution for 10 min at different temperatures. (a) Room temperature; (b) 80 °C

potentials for 20 s and then immersed under OCP for 40 s. With applying different potentials, the width of the oxide rings was apparently changed. The more negative potential from OCP was applied, the thinner the oxide rings was. For example, when the applied potential was  $-0.3$  V vs. OCP, the width of the string-like oxide ring (See Fig. 11) was narrowed down to an averaged value of  $2.19$   $\mu\text{m}$ , which is extremely thinner compared to the width of  $11.80$   $\mu\text{m}$  at OCP in deionized water. Two reasons could govern the thinned oxide rings under a negative potential. First, under a strengthened, intermittent cathodic polarization, the reduction reaction of oxygen relied on the supply and the consumption of dissolved oxygen during the inward diffusion from the bulk solution to the reactive core

region, resulting in an obviously localized distribution of hydroxide concentration. Second, a deficiency of  $\text{Fe}^{2+}$  ion combined with a localized, concentrated  $\text{OH}^-$  ion over the NdFeB surface could generate a sharply narrowed oxide ring. From the results, a positive potential from OCP could produce more  $\text{Fe}^{2+}$  ion and a slightly concentrated gradient of  $\text{OH}^-$  ion, widening the oxide rings.

**3.4.5 pH Value.** To testify the localization of cathode reactions during corrosion, the solution pH was controlled at 10 to generate highly concentrated and uniformly distributed  $\text{OH}^-$  ion on the NdFeB surface. After immersion in this alkaline solution for 10 min, the oxide rings were also observed as shown in Fig. 12, but they were obviously more diffusive,

much weaker than those formed in the normal conditions (see Fig. 5, 7, 9 and 10). The mean radius of the oxide rings expands to  $48.17 \mu\text{m}$ , significantly larger than that observed in neutral deionized water ( $32.5 \mu\text{m}$ ). The high concentration of  $\text{OH}^-$  ion in alkaline solution can ease the formation of iron oxide at a low concentration limit of  $\text{Fe}^{2+}$  ion. We also noticed that the improved conductivity in alkaline solution is also a possible reason for the expended oxide rings. Compared with the polarization conditions in Sect. 3.4.4, it can be deduced that the distributions of  $\text{OH}^-$  and  $\text{Fe}^{2+}$  ions over the NdFeB surface probably determine the width of the oxide rings. The distribution of  $\text{Fe}^{2+}$  in the solution over the surface was a function of the anodic dissolution rate from the pitting, which was primarily determined by the acidity of the solution inside the pit rather than the solution outside the pit. Therefore, the deposition of corrosion products was to some extent controlled by the distribution of the hydroxide concentration or the solution pH. In this case, a homogeneous distribution of  $\text{OH}^-$  ion would generate a wide, diffusive oxide ring, while a localized enrichment of  $\text{OH}^-$  ion produce a narrowed oxide ring. Obviously, the width of the oxide ring was a result of the distributions of  $\text{Fe}^{2+}$  and  $\text{OH}^-$  ions, where  $\text{OH}^-$  ion plays the key role.

## 4. Discussion

### 4.1 Spatial Separation of Anode and Cathode

The anode region was actively dissolved during immersion, resulting in the formation of corrosion pits or craters on NdFeB alloy surfaces. At the cathode region, the corrosion products were deposited on NdFeB surface. Generally, the anode and cathode regions are varied with time, while they are spatially

separated in some cases. For example, in an Evans droplet, the oxygen gradient in the solution induces the significant spatial separation of the anode and the cathode on the metal surface (Ref 24, 25). The droplet/air interface region is saturated with oxygen, serving as the cathode area. The center of droplet is deficient in oxygen, where the steel surface becomes active, developing as the anode area during corrosion. In the immersion test of NdFeB samples, oxygen is homogenous in the bulk solution and there is no oxygen gradient at the sample surface. Although their surface morphologies are similar, the localized corrosion of NdFeB alloy in immersion conditions is not exactly the same as the Evans droplet corrosion.

We tried to explain the formation of oxide rings on NdFeB surfaces by using the potential-pH diagram. Figure 13 shows the potential-pH diagram of Fe- $\text{H}_2\text{O}$  system. The free corrosion potential of NdFeB alloy in deionized water is  $-0.28 \text{ V}$  vs. SCE, and the pH of deionized water is about 6.62. When NdFeB alloy was immersed in deionized water, some active points in the Fe-rich main phase near to the phase boundaries close to a Nd-rich particle would be preferentially dissolved due to the well-known galvanic effect. At the anode area, the reactions include the oxidation of Fe or Nd atoms and the hydrolysis of  $\text{Fe}^{2+}$  or  $\text{Nd}^{3+}$  ions. Here, the fraction of Nd in the original alloy was very small, resulting in no detectable signals from Nd oxides in the Raman spectra. As an example, the reactions associated with Fe were illustrated as (1) and (2).



Therefore, the production of  $\text{H}^+$  Eq. 2 around the anode region would lead to a local potential drop and an acidification (a decrease of the pH value), resulting in the local environment

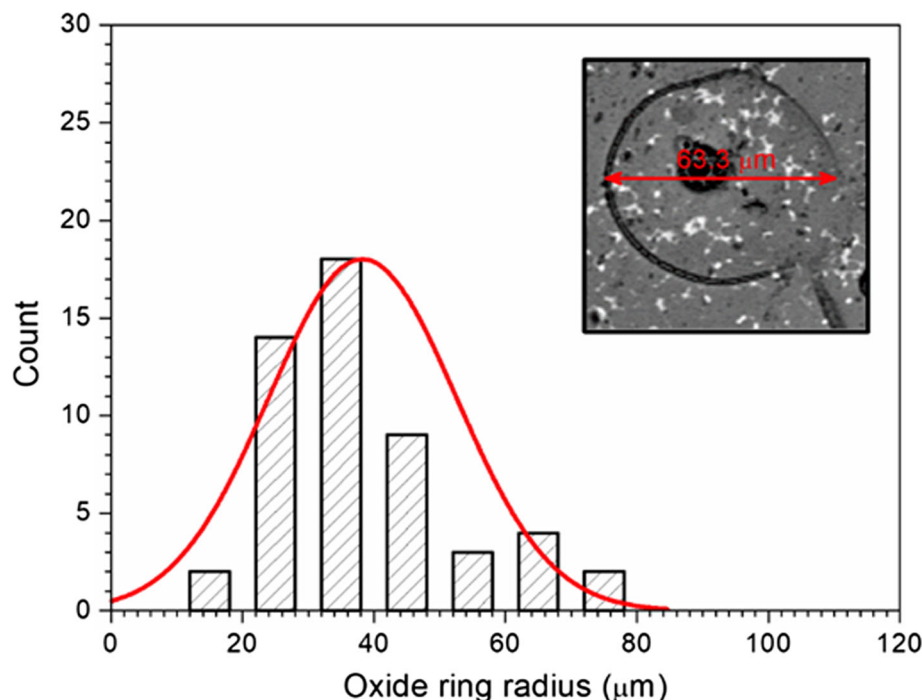


**Fig. 11** Histogram of the oxide ring radius on NdFeB alloy surfaces after alternating polarization test at  $-0.3 \text{ V}$  vs. OCP for 10 cycles and the typical illustration of a single oxide ring (inserted SEM image)

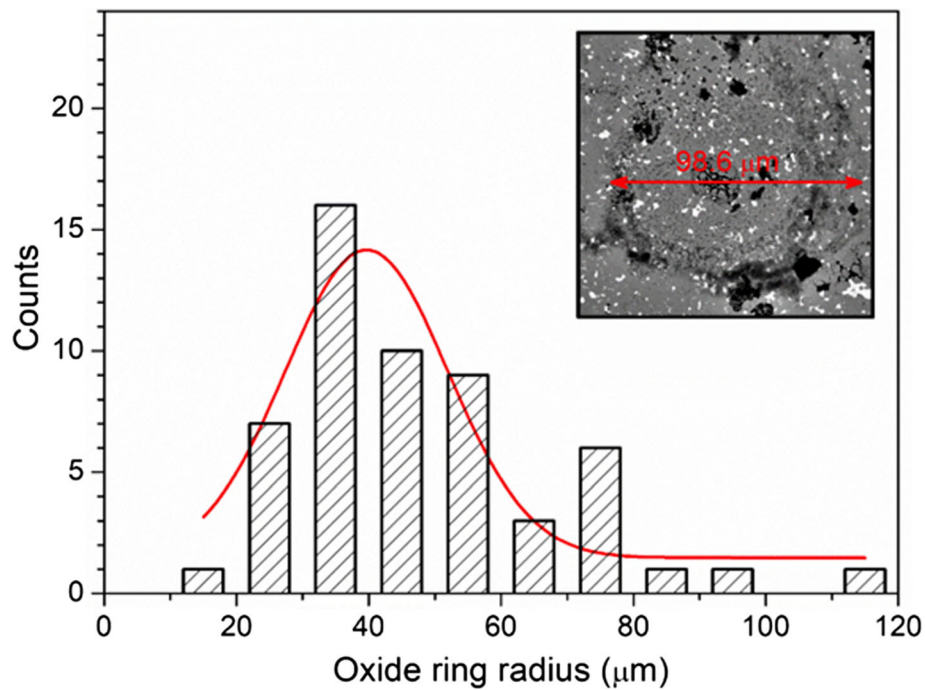


**Fig. 12** Histogram of the oxide ring radius on NdFeB alloy surfaces after immersion in NaOH solution with a pH value of 10 for 10 min and the typical illustration of a single oxide ring (inserted SEM image)

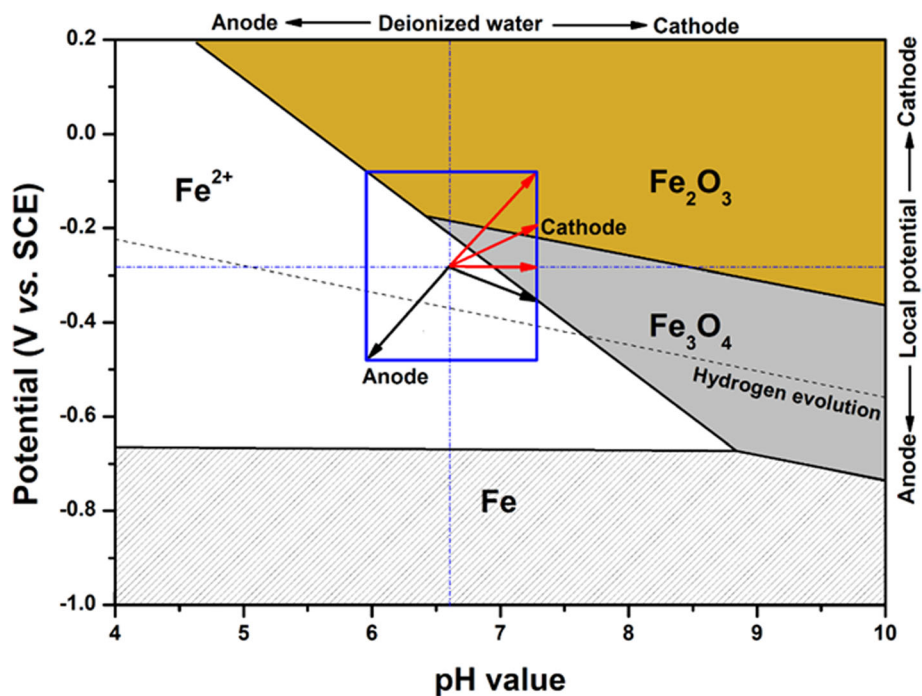


**Fig. 13** Potential-pH diagram of Fe-H<sub>2</sub>O system and the environmental variations on NdFeB alloy surfaces during corrosion

away from the solid-state region and the formation of soluble corrosion products (such as Fe<sup>2+</sup> ion) as illustrated in Fig. 13.

At the same time, the cathode region, particularly the Nd-rich particle containing areas next to the anode, would become alkaline with the generation of OH<sup>-</sup> ion or the consumption of H<sup>+</sup> ion. The reaction can be expressed as Eq (3) and (4).



The local environment in the cathode region surrounding the anode would be significantly affected by the anode. It should be

noted that the intensive anodic dissolution in the pit could not be fully balanced by the cathodic reactions outside the pit through galvanic effect. Rapid cathodic reactions would also occur inside the pit, which could significantly consume the oxygen from the surrounding region and the intensity of the cathodic process outside the pit could not balance the excess of anodic reaction within the pitted region. Therefore, thick corrosion products could not be loosely deposited in this zone due to the lack of hydroxide ions, although there was a high concentration of ferrous ions there from the pit. Consequently, there would be a smooth blank region without visible corrosion products between anode and cathode. In the area some distance away from the anode region, the oxygen concentration in the solution resumed to the normal level, and the cathode oxygen reaction rate increased. Outside the pitting affected region, the  $\text{OH}^-$  generation rate was increased, while less  $\text{Fe}^{2+}$  ions were arrived from the pits. Eventually, the concentration product of  $\text{OH}^-$  and  $\text{Fe}^{2+}$  would meet the deposition condition somewhere between the pit and cathodic region, forming a corrosion product ring. There is no doubt that the increasing pH value and the decreasing ferrous ion concentration with the distance from the pit induced the formation of oxide rings. It should also be noted that the cathode reactions producing a high concentration of  $\text{OH}^-$  ions did not necessary take place over these oxide rings on the NdFeB surface, because the deposition of corrosion products could to some degree reduce the cathodic reactions, and the adjacent areas without deposition or the corrosion products could immediately become the primary cathode in the corrosion process.

#### 4.2 Localization of Cathode Reactions

The potential-pH diagram can thermodynamically predict the presence of a blank region just around the anode regions. Obviously, the formation of oxide rings is also a kinetic process. The size, width and shape of the oxide rings are dependent on the release and diffusion of ionic species of  $\text{Fe}^{2+}$  and  $\text{OH}^-$ , which are generated from the anode and cathode reactions, respectively. The deposition reaction is governed by the solubility product of  $\text{Fe}(\text{OH})_2$ , which is related to  $[\text{Fe}^{2+}] \times [\text{OH}^-]^2 = K_{\text{sp}}$ . Generally,  $K_{\text{sp}}$  is a constant at a certain environment. When the concentrations of  $\text{Fe}^{2+}$  and  $\text{OH}^-$  exceed the solubility limits, solid corrosion products would be deposited on NdFeB surfaces. At places adjacent to the anode region,  $\text{Fe}^{2+}$  is sufficient, but  $\text{OH}^-$  is extremely deficient, leading to the formation of a blank region. At the cathode region, where locates away from the anode region, the deposition of  $\text{Fe}(\text{OH})_2$  is related to  $\text{OH}^-$  generation and  $\text{Fe}^{2+}$  diffusion.

The size and width of the oxide rings were determined by the diffusion and accumulation of ionic species adjacent to the NdFeB surfaces.  $\text{Fe}^{2+}$  ion was continuously released from the anode region and was diffused away under the concentration gradient just above the surface. Given sufficient long time, the concentration of  $\text{Fe}^{2+}$  ion at a certain point away from the anode area steadily increased and nearly reached a steady state if not consumed by combination with hydroxide and deposition. In this case, the deposition of iron oxides on NdFeB surface would mainly be governed by the variation of local pH value. In the anode protected zone, the strong galvanic protection and the deficient of oxygen led to the blank region formed surrounding the pits. Since cathode reactions would induce an increase in pH value, which facilitated the deposition

of iron oxides when sufficient ferrous ions present in the solution, the ring-shaped distribution of iron oxides possibly revealed that the concentration of the generated  $\text{OH}^-$  ions by cathode reactions had been high enough to combine with the dissolved  $\text{Fe}^{2+}$  in such a circular region. As seen from Fig. 12, when  $\text{OH}^-$  ion was homogeneously distributed on NdFeB surfaces by addition of NaOH, the iron oxide was widely dispersed. On the opposite side, when the NdFeB surface was temporarily polarized to a negative potential (Fig. 11), the iron oxides were deposited as circular stringers, indicating a higher intensity of cathode reactions in some local areas.

The spatial location of the oxide deposits may be dependent on the solution conductivity, as the ion transportation can be enhanced by the electric field between the anode and cathode in an electrochemical system. However, as seen from Fig. 8, the radius of the oxide rings seems unchanged in a wide range of solution conductivity, which possibly indicates that  $\text{Fe}^{2+}$  diffusion or transportation is mainly controlled by the concentration gradient, rather than the local buildup of electric fields between the anode and the cathode. Given enough time, the ionic difference between the spatially separated anode and cathode could keep neutrality. It generally needs several minutes to observe the oxide rings on NdFeB surface. Before the formation of oxide rings, the dissolved oxygen within the developing anode region was quickly exhausting and the cathode reactions were randomly happening. After the anode region became stable, excessive  $\text{Fe}^{2+}$  ion would be diffused away and the reduction of oxygen and water would be inhibited.

There are two reasons for determining the location of the abnormal intensive cathode reactions some distance from the anode region. Firstly, oxygen concentration in the bulk solution controls the rate of oxygen diffusion and the cathode reaction (Fig. 9). A higher oxygen concentration provides larger spatial edges of cathode reactions. The temperature dependence also confirms the oxygen influence on the radius of the oxide rings. Second, the distribution of the surface corrosion product film on the alloy may locally alter the intensity of cathode reactions. The surface area covered by the film is relatively inactive for cathode reactions. The absence of iron oxide deposits on Nd-rich phase confirms the influence of the film on the formation of oxide rings.

#### 4.3 Model for the Corrosion Morphology

A simple model for the galvanic corrosion on NdFeB surface was established, as shown in Fig. 14. The localized corrosion morphology on NdFeB alloy surface includes four regions: A is the anode region, B is the blank region, C is the cathode region, and D is the distant region. The anode region is resulted from the active dissolution of matrix phase adjacent to the phase boundaries, leaving a crater on the NdFeB surface. The high concentration of  $\text{Fe}^{2+}$  released during anode dissolution reduces the pH value around the growing craters. According to the E-pH diagram of Fe- $\text{H}_2\text{O}$  system, Fe in region B is mainly in the form of soluble salts composed of  $\text{Fe}^{2+}$ ,  $\text{Fe}^{3+}$  and  $\text{HFeO}_2$ , without the deposition of corrosion products. In the initial stage of corrosion, oxygen around the anodic region can be quickly exhausted, because the intensive anodic dissolution in the pit needs to be balanced by cathodic reaction locally and spontaneously. After the initial period, diffusion of oxygen from bulk solution to such a local active area controls the cathode reactions. Oxygen is deficient for the reduction

reactions. In this case, in region C the pH would increase to a value high enough while the concentration of the ferrous ions diffused from the pitting is not too low to form iron oxides. The diffusion flows of the hydroxide anion from farther area and the ferrous cations from the pit can just sustain the deposition of oxides in zone C, producing a ring-shaped deposition of corrosion products there. Initially, the cathodic  $\text{OH}^-$  generation reaction may mainly occur in zone C, while in zone D the cathodic reaction is relatively weak. Figure 14 mainly illustrates the processes in this moment. However, as more and more corrosion products are deposited in zone C, the cathodic  $\text{OH}^-$  generation reaction will be suppressed by the deposition. To balance the anodic current from the pit, the cathodic reaction will be shifted to zone D. Then the  $\text{OH}^-$  generated from Zone D will meet with the ferrous cation from the pit on zone C to form deposits there. In this stage, the reactions over the electrode surface can be impeded by corrosion products, which may result in relatively instable EIS data points (Fig. 3d). Eventually, the cathodic reaction will dominate in zone D where the ferrous ion concentration is always too low to form corrosion products. Therefore,  $\text{OH}^-$  and  $\text{Fe}^{2+}$  can only continuously diffuse opposingly, forming corrosion products in region C. Therefore, the oxygen-diffusion controlled  $\text{OH}^-$  ion generation from farther area, together with the ferrous cation anodically dissolved from the pit, determines the location of the oxide throughout the immersion test.

#### 4.4 Perspectives on Galvanic Corrosion

It was generally believed that the phase heterogeneities governed the corrosion resistance of NdFeB alloys. The active phases or phase boundaries are preferentially dissolved away, servicing as the anode. The inert phases perform as the cathode. Galvanic coupling between the active and inert parts on NdFeB surface would accelerate the electrochemical corrosion process, presenting a “small anode and big cathode” scenario. The distribution of Nd-rich phase is the key to determine corrosion of NdFeB alloys.

In deionized water, the corrosion process of sintered NdFeB alloys slows down, capturing the initial stage of the galvanic corrosion. Similar to an Evans droplet, it shows a spatial separation of the anode and the cathode. Interestingly, the cathode reaction of oxygen reduction mainly concentrates in a ring-shaped region away from the anode region on NdFeB alloy surface, other than the whole inert matrix phase. It is clear that the alloy heterogeneity mainly determines the location of anode pits or craters, while the spatial distribution of cathode reactions results from the local environmental variations. Similar observations have also been made in Al-based alloys, where the corrosion products are deposited in rings around the deep pits as a result of the cooperative corrosion among active intermetallic phases (Ref 29, 30). However, in current study the Nd-rich phase was widely distributed and no Nd-phase clusters could be identified within the oxide rings. Diffusion of dissolved oxygen seems to limit the localization of cathode reactions. The diffusion of hydroxide and ferrous ions in the solution plays a key role in determining the corrosion morphologies. A method to slow down the diffusion of oxygen or improve the protectiveness of the surface corrosion product film on the surface is possibly effective for mitigating localized corrosion of a NdFeB alloy.

## 5. Conclusions

The corrosion behavior of sintered NdFeB alloy was investigated by using quasi-in situ SEM observation in low-conductive aqueous solutions to slow down its corrosion process. The initial stage of localized corrosion on NdFeB alloy surface was clearly explored. The following conclusions can be drawn:

- (1) In deionized water, corrosion pits started from the phase boundaries, particularly next to the Nd-rich phase particles, and propagated in the matrix phase, owing to the improved stability of the oxide-covered Nd-rich phase.

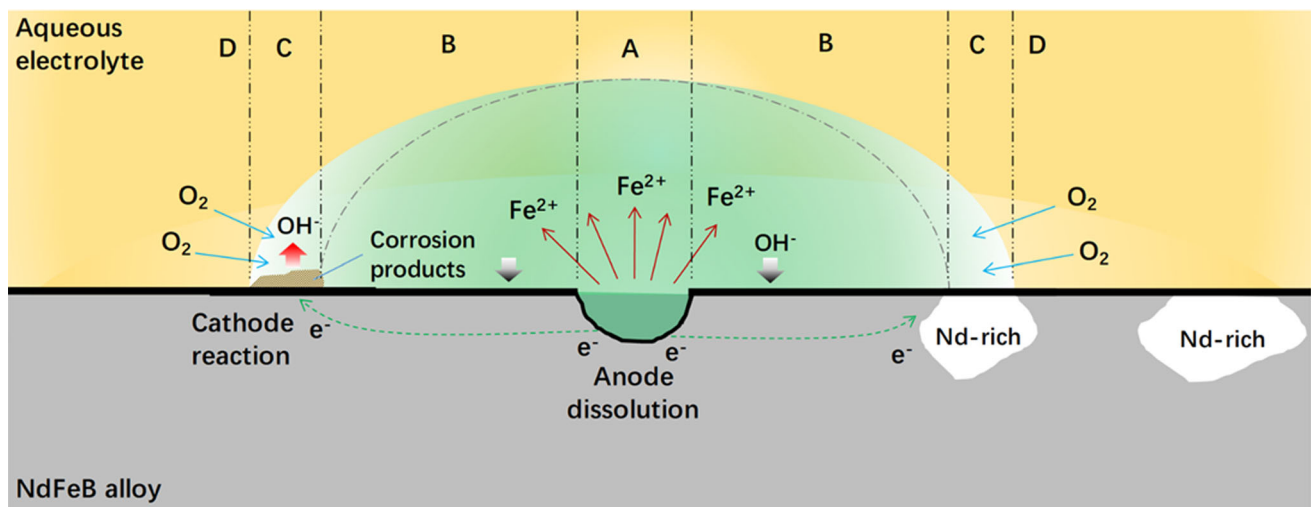


**Fig. 14** Schematic illustration of the propagation of micro-galvanic corrosion on NdFeB alloy surface in the initial stage when the corrosion products deposited in Zone C cannot effectively suppress the oxygen reduction reaction. In the later stage, as more and more corrosion products are deposited in Zone C, the oxygen reduction will be inhibited. To balance the anodic current from the pit, the oxygen reduction will be shifted to zone D. Then the  $\text{OH}^-$  generated from Zone D will meet with the ferrous cation from the pit in Zone C and continuously form deposition on the surface in Zone C

- (2) Oxide rings were formed on the NdFeB alloy surface some distance away from the pitting points, and their size and width were influenced by environmental factors. The formation of the oxide rings was influenced the non-uniformly distributed cathode reactions on the NdFeB alloy surface or spatially separated anode and cathode in corrosion.
- (3) Four regions of the corrosion morphology could be identified on the NdFeB alloy surface: anode region, blank region, deposition region and the distant region. The localization of cathodic reactions was determined by the limited diffusion of oxygen from the bulk solution and the deposition of corrosion products on the alloy.

## Acknowledgments

This work was supported by the Science and Technology Planning Project of Fujian Province (No. 2018H6017) and the Fundamental Research Funds for the Central Universities (No. 20720210052). We also acknowledged Mr. Linshe Shi at Xiamen Tungsten Co. Ltd. for providing the sintered NdFeB alloy samples.

## References

1. A.S. Kim and F.E. Camp, High Performance NdFeB Magnets, *J. Appl. Phys.*, 1996, **79**, p 5035–5039
2. F. Vial, F. Joly, E. Nevalainen, M. Sagawa, K. Hiraga, and K.T. Park, Improvement of Coercivity of Sintered NdFeB Permanent Magnets by Heat Treatment, *J. Magn. Magn. Mater.*, 2002, **242**, p 1329–1334
3. Y. Kim, H. Yuk, R.K. Zhao, S.A. Chester, and X.H. Zhao, Printing Ferromagnetic Domains for Untethered Fast-transforming Soft Materials, *Nature*, 2018, **558**, p 274–279
4. E. Chen, K. Peng, W.L. Yang, J.J. Zhu, D.Y. Li, and L.P. Zhou, Effects of Al Coating on Corrosion Resistance of Sintered NdFeB Magnet, *Trans. Nonferr. Metals Soc. China*, 2014, **24**, p 2864–2869
5. A. Ali, A. Ahmad, and K.M. Deen, Multilayer Ceramic Coating for Impeding Corrosion of Sintered NdFeB Magnets, *J. Rare Earths*, 2009, **27**, p 1003–1007
6. Y. Wang, Y.Z. Deng, Y.T. Ma, and F. Gao, Improving Adhesion of Electroless Ni-P Coating on Sintered NdFeB Magnet, *Surf. Coat. Technol.*, 2011, **206**, p 1203–1210
7. X. Zhang, Y.T. Ma, B. Zhang, Y. Li, M.K. Lei, F.H. Wang, M.G. Zhu, and X.C. Wang, Corrosion Behavior of Hot-pressed Nanocrystalline NdFeB Magnet in a Simulated Marine Atmosphere, *Corros. Sci.*, 2014, **87**, p 156–166
8. P.J. Zhang, M.G. Zhu, W. Li, G.Q. Xu, X.L. Huang, X.F. Yi, J.W. Chen, and Y.C. Wu, Study on Preparation and Properties of CeO<sub>2</sub>/epoxy Resin Composite Coating on Sintered NdFeB Magnet, *J. Rare Earths*, 2018, **36**, p 544–551
9. J. Fidler, Analytical Microscope Studies of Sintered Nd-Fe-B Magnets, *IEEE Trans. Magn.*, 1985, **21**, p 1955–1957
10. A.A. El-Moneim and A. Gebert, Electrochemical Characterization of Galvanically Coupled Single Phases and Nanocrystalline NdFeB-based Magnets in NaCl Solutions, *J. Appl. Electrochem.*, 2003, **33**, p 795–805
11. W.Q. Liu, M. Yue, J.X. Zhang, G.P. Wang, and T. Li, The Effect of Nd-rich Phase for Sintered NdFeB Corrosion Resistance, *Rare Metal Mater. Eng.*, 2007, **36**, p 1066–1069
12. D.F. Cygan and M.J. McNallan, Corrosion of NdFeB Permanent-Magnets in Humid Environments at Temperatures up to 150 °C, *J. Magn. Magn. Mater.*, 1995, **139**, p 131–138
13. A.A. El-Moneim, Passivity and its Breakdown of Sintered NdFeB-based Magnets in Chloride Containing Solution, *Corros. Sci.*, 2004, **46**, p 2517–2532
14. K.K. Zhang, E.D. Fan, J. He, X.G. Li, and Y.H. Huang, Long-term Effects of Electrochemical Corrosion on Magnetic Properties of Sintered NdFeB Magnets, *J. Magn. Magn. Mater.*, 2021, **538**, p 168309
15. H. Bala, G. Pawlowska, S. Szymura, and Y.M. Rabinovich, Electrochemical Corrosion Characterisation of Intermetallic Phases Occurring in Nd-Fe-B Type Magnets, *Br. Corros. J.*, 1998, **33**, p 37–41
16. E. Isotahdon, E. Huttunen-Saarivirta, S. Heinonen, V.T. Kuokkala, and M. Paju, Corrosion Mechanisms of Sintered Nd-Fe-B Magnets in the Presence of Water as Vapour, Pressurised Vapour and Liquid, *J. Alloy. Compd.*, 2015, **626**, p 349–359
17. L. Schultz, A.M. El-Aziz, G. Barkleit, and K. Mummert, Corrosion Behaviour of Nd-Fe-B Permanent Magnetic Alloys, *Mat Sci Eng a-Struct.*, 1999, **267**, p 307–313
18. M.X. Bi, C. Xu, A.G. Wattoo, R. Bagheri, Y.X. Chen, S.D. Mao, Z.S. Lv, L.J. Yang, and Z.L. Song, Corrosion Behavior of Sintered CeNdFeB Magnets in Different Solutions, *J. Alloy. Compd.*, 2017, **703**, p 232–241
19. K. Chitrada, K.S. Raja, B. Pestic, and I. Chant, Corrosion Behavior of Surface Modified NdFeB Permanent Magnet in Dilute Chloride Environments, *Electrochim. Acta*, 2014, **123**, p 23–32
20. G.L. Yan, A.J. Williams, J.P.G. Farr, and I.R. Harris, The Effect of Density on the Corrosion of NdFeB Magnets, *J. Alloy. Compd.*, 1999, **292**, p 266–274
21. G.W. Warren, G. Gao, and Q. Li, Corrosion of NdFeB Permanent Magnet Materials, *J. Appl. Phys.*, 1991, **70**, p 6609–6611
22. T.E. Standish, L.J. Braithwaite, D.W. Shoesmith, and J.J. Noel, Influence of Area Ratio and Chloride Concentration on the Galvanic Coupling of Copper and Carbon Steel, *J. Electrochem. Soc.*, 2019, **166**, p C3448–C3455
23. G.L. Yan, P.J. McGuinness, J.P.G. Farr, and I.R. Harris, Environmental Degradation of NdFeB Magnets, *J. Alloy. Compd.*, 2009, **478**, p 188–192
24. S.X. Li and L.H. Hihara, In situ Raman Spectroscopic Identification of Rust Formation in Evans' Droplet Experiments, *Electrochem. Commun.*, 2012, **18**, p 48–50
25. R.J. Jiang and Y.F. Cheng, Mechanism of Electrochemical Corrosion of Steel under Water Drop, *Electrochem. Commun.*, 2013, **35**, p 8–11
26. L. Yang, Z.M. Wang, L.S. Shi, D.J. Zheng, D.H. Fu, and G.L. Song, Copper Ion Accelerated Local Failure of Epoxy Coating on NdFeB Magnet in Immersion Conditions, *Eng. Fail. Anal.*, 2020, **115**, p 104677
27. H. Yang, S. Mao, and Z. Song, The Effect of Absorbed Hydrogen on the Corrosion Behavior of Sintered NdFeB Magnet, *Mater. Corros. Werkst. Und Korros.*, 2012, **63**, p 292–296
28. L.Q. Yu, Y.H. Wen, and M. Yan, Effects of Dy and Nb on the Magnetic Properties and Corrosion Resistance of Sintered NdFeB, *J. Magn. Magn. Mater.*, 2004, **283**, p 353–356
29. A.E. Hughes, A. Boag, A.M. Glenn, D. McCulloch, T.H. Muster, C. Ryan, C. Luo, X. Zhou, and G.E. Thompson, Corrosion of AA2024-T3 Part II Co-operative Corrosion, *Corros. Sci.*, 2011, **53**, p 27–39
30. Y. Ma, X. Zhou, W. Huang, G.E. Thompson, X. Zhang, C. Luo, and Z. Sun, Localized Corrosion in AA2099-T83 Aluminum-Lithium Alloy: The Role of Intermetallic Particles, *Mater. Chem. Phys.*, 2015, **161**, p 201–210

**Publisher's Note** Springer Nature remains neutral with regard to jurisdictional claims in published maps and institutional affiliations.

Springer Nature or its licensor (e.g. a society or other partner) holds exclusive rights to this article under a publishing agreement with the author(s) or other rightsholder(s); author self-archiving of the accepted manuscript version of this article is solely governed by the terms of such publishing agreement and applicable law.